# Influence of Gold Nano-bipyramid Dimensions on Strong Coupling with Excitons of Monolayer MoS$_2$

Julia Lawless[1], Calin Hrelescu[1], Carolyn Elliott[1,2], Lisanne Peters[3], Niall McEvoy[3] and A. Louise Bradley[1,2]*

1. School of Physics and AMBER, Trinity College Dublin, College Green, Dublin 2, Ireland
2. IPIC, Tyndall National Institute, Cork, Ireland
3. School of Chemistry and AMBER, Trinity College Dublin, College Green, Dublin 2, Ireland

ABSTRACT: Rabi splitting between the longitudinal plasmon of a gold nano-bipyramid and the A exciton of monolayer MoS$_2$ is observed at room temperature. The dependence of the Rabi splitting on the physical dimensions of the nano-bipyramid is reported. The impact of bipyramid length, aspect ratio and tip radius on the coupling strength are investigated. The mode volume of the nanoresonator is significantly reduced due to the sharp tips of the bipyramid, and the Rabi splitting increases with tip sharpness. The results also reveal that greater Rabi splitting is observed for larger bipyramids, contrasting with results perviously reported for different nanoresonator shapes. This shows, for the first time, how the magnitude of the splitting has a different response for particular nanoresonators when tuning the size, without increasing the number of excitons coupled into the system. The Rabi splitting, at zero energy detuning between plasmon and A exciton, increases from ~ 55 meV with a 70 nm long bipyramid to ~ 80 meV with a 100 nm long bipyramid. The increase in coupling strength with size arises due to increasing confinement of the field enhancement at the bipyramid tip.
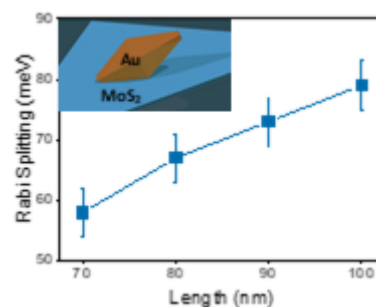
Introduction

In the strong coupling regime, the rate of coherent energy exchange between a quantum emitter and an optical resonator mode is quicker than their intrinsic dissipation rates. In contrast to the weak coupling regime, known as the Purcell effect[1], the energy of the strongly coupled system is not only enhanced or quenched but splits into two entirely new eigenstates (polaritons). This so-called Rabi splitting has a large range of applications.[2] These include the control of chemical reactions and modification of the chemical reaction rates,[3–5] applications in low threshold lasers,[6] optical switching[7] and quantum information processing.[8] An in-depth understanding of the conditions necessary to achieve strong coupling with nanostructures is crucial to pave the road towards technological applications of plasmon−exciton strong coupling.

Previously, the observation of strong coupling was limited to experiments at cryogenic temperatures.[9–13] With the development of nanoscience, various photonic and plasmonic nanostructures were used to achieve strong coupling at room temperature without the need for a closed optical cavity.[13–18] For instance, strong coupling was observed in nanosystems consisting of a large quantity of randomly oriented J aggregates interacting with the modes of plasmonic nanostructures.[19–21]

As an alternative to J aggregates, transition metal dichalcogenides (TMDCs) have shown themselves to be an excellent platform for achieving Rabi splitting.[14,16,22–28] In the bulk, they are a stack of two-dimensional layers, held together by van der Waals forces.[29,30] In the single-layer limit, TMDCs exhibit different optical properties, with many transitioning from an indirect to a direct band-gap.[31,32] In particular, monolayers of TMDCs have tightly bound excitons with high oscillator strengths, due to high quantum confinement. This arises as the thickness of the monolayer is smaller than the Bohr radius.[33–36] TMDC monolayers are of particular interest for optoelectronic applications since their optical properties are relatively stable and can be tuned with various methods, including electrically.[16,37] Strong coupling has been achieved with many systems involving TMDCs as the quantum emitter,[38] including, for example a layer of a TMDC in a microcavity with the cavity thickness used to tune the coupling.[23,39,40] Lattices of plasmonic nanoparticles have also been used to investigate Rabi splitting, with the particle size and the lattice constant both used to tune the plasmonic resonances.[23,41,42]

A variety of investigations have been carried out to study the strong coupling of individual plasmonic nanoparticles with TMDCs on a substrate,[16,43,44] allowing for a more detailed examination of the interaction of a few excitons with the confined optical modes. Such studies are of major interest for quantum optics. However, the excitons of TMDC monolayers have a high in-plane dipole transition moment but extremely reduced or non-existent out-of-plane dipole moments. Consequently, in several nanoparticle TMDC systems, such as particle-on-film configurations, nanoparticle dimer, spherical particles and even nanorods on TMDC monolayers, the local electric field and the dipole moment are far from being colinear. This misalignment
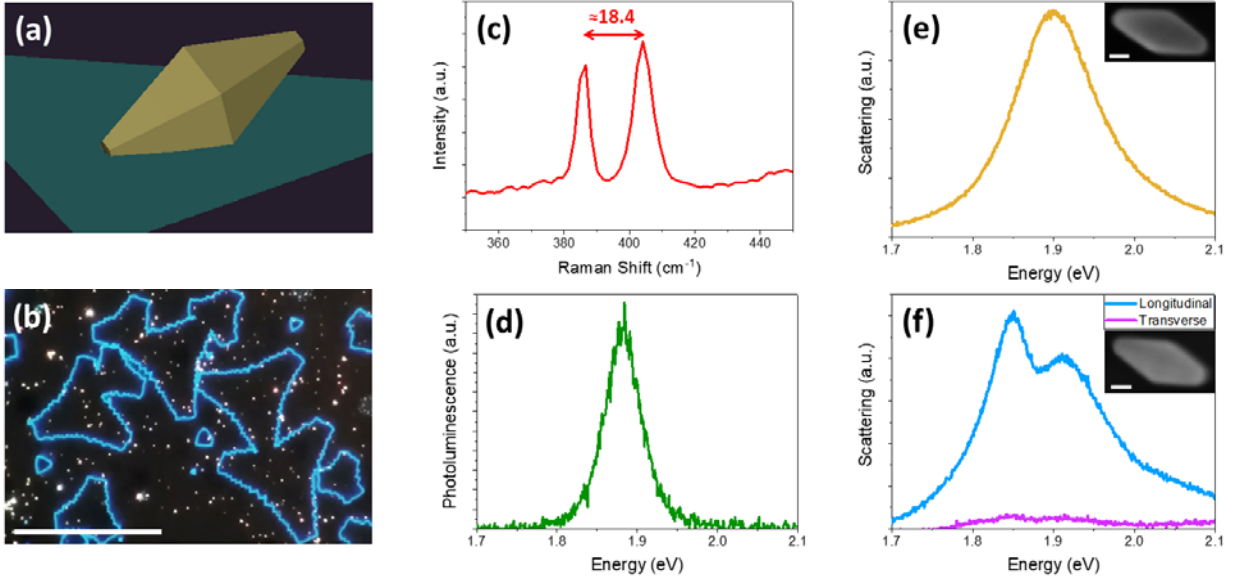
Figure 1. (a) Schematic showing a single Au bipyramid lying on a MoS$_2$ flake on a SiO$_2$/Si substrate. (b) Dark field microscopy image of Au bipyramids on MoS$_2$ flakes (white scale bar shows 50 µm). (c) and (d) Typical Raman and PL spectra of MoS$_2$ flakes used. (e) Scattering spectrum of a single bipyramid directly on a SiO$_2$/Si substrate. (f) Polarization resolved scattering spectra of a single Au bipyramid on monolayer MoS$_2$. Insets show corresponding SEM images (white scale bars show 20 nm).

can make strong coupling between plasmonic nanoparticles and monolayers impossible.[28] Additionally, other reports on strong coupling between single metal nanoparticles and quantum emitters have found that the coupling strength decreases with increased metal volume of the nanoparticle[16,17] but little research has been conducted to find if this remains true for varying particle shapes.

Recently, Stührenberg et al.[14] reported on an elegant method to overcome the misalignment between the local fields induced by nanoparticles and the in-plane dipole moments of the TMDC monolayers using nanoparticles with bipyramidal shape. In that case the dependence of the Rabi splitting on the aspect ratio of the bipyramids and the number WSe$_2$ layers was investigated. Rabi splitting greater than 100 meV was reported for Au bipyramids on mono- and multilayer WSe$_2$.

Motivated by the report of Stührenberg et al.,[14] we investigate the interaction of the A excitons of a MoS$_2$ monolayer with gold nano-bipyramids. MoS$_2$ was chosen as the TMDC to couple to the bipyramids in this system due to the lower temperatures required for its synthesis compared with WSe$_2$,[45] as well as its A exciton energy being within the visible range.[29,46] The dependence of the strong coupling between the longitudinal plasmon of the Au bipyramids and the A exciton of the monolayer of MoS$_2$ for varying bipyramid lengths is measured at single nanoparticle level. We present new insights on how the tip radii and overall bipyramid size affect strong coupling, since nano-bipyramids on TMDC monolayers are the ideal candidates to enable the investigation of few excitons strongly coupled to the spatially confined optical mode, i.e. the electric field enhancement in the hot spot at the tips of the bipyramid (as suggested by Stührenberg et al.[14]). Here we present evidence showing that in the case of bipyramid nanoresonators the coupling strength increases with a higher metal volume, due to the electric field enhancement at the tip of the larger bipyramids. This is in contrast to previous reports where the coupling strength decreases with increased metal volume of the nanoresonator[16,17]

The coupled oscillator model can be used to describe the strong coupling system. In a strongly coupled system, the plasmon and exciton hybridise into two new energetical eigenstates, namely the upper and lower polariton. The energies of the upper and lower polaritons (ω_{up} and ω_{lp} respectively) are given by the following equation[13,47]

$$\omega_{up/lp} = \frac{\omega_{pl} + \omega_{ex}}{2} \pm \sqrt{g^2 + \frac{1}{4}\left[\Delta\omega - \frac{i}{2}(\Delta\gamma)\right]^2} \quad (1)$$

where ω_{ex} is the energy of the A exciton, ω_{pl} is the energy of the plasmon, g is the coupling strength, $\Delta\omega = \omega_{pl} - \omega_{ex}$ is the energy detuning and $\Delta\gamma = \gamma_{pl} - \gamma_{ex}$, where γ_{pl} is the plasmon dissipation rate and γ_{ex} is the exciton dissipation rate.

Gold nano-bipyramids offer several advantageous properties to achieve strong coupling. The longitudinal plasmon resonance of Au nano-bipyramids can be easily tuned to overlap with the energy of the A exciton by varying dimensions of the bipyramid. A spectrally sharp plasmon resonance, which is equivalent to a low plasmon dissipation rate γ_{pl}, is important for strong coupling, since the coupling strength g must exceed both, the plasmon and the exciton dissipation rate[15,48–52]

$$g > \gamma_{pl}, \gamma_{ex} \quad (2)$$

Another important effect of the shape of the bipyramids is their tuneable, sharp tips, causing a large localization of the electric field and a substantial field enhancement at the tips. This provides the opportunity to increase the coupling strength.[17,19,53] The sharp tips also offer the ideal platform for reducing the mode volume of the resonator. On a substrate only one of ten facets of the bipyramid touches the surface (see figure 1a). This further reduces the mode volume of the resonator as only one sharp tip is in contact with the TMDC monolayer, and hence only one hot spot interacts with the quantum emitter. The coupling constant, g, depends on the mode volume as described by the following equations:[9,10,13]

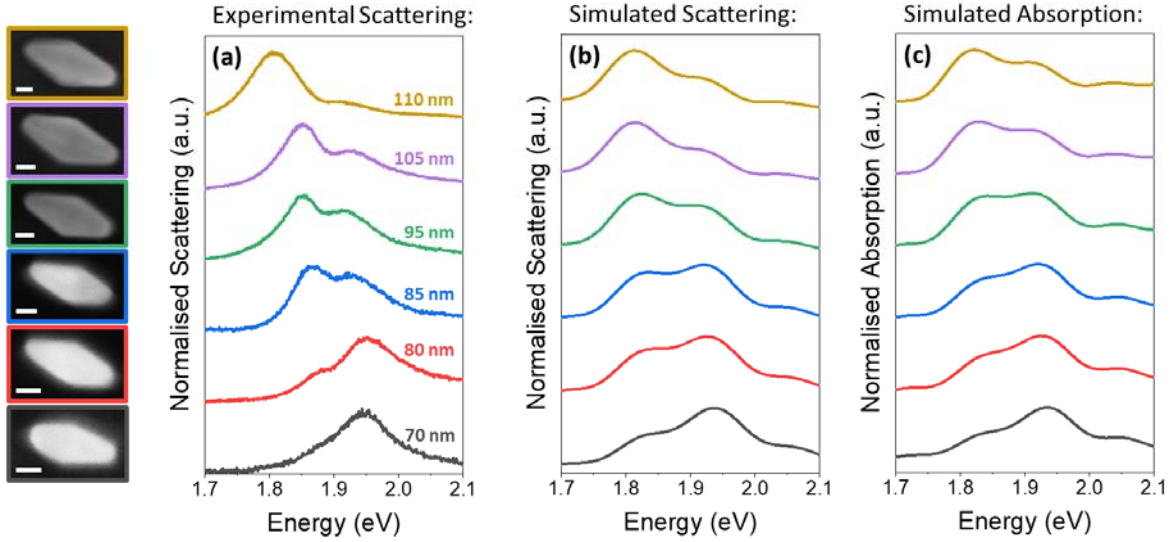$$g = \sqrt{N}\mu_e|E_{vac}| \quad (3)$$

Figure 2. (a) Experimental scattering from Au bipyramids of varying lengths with aspect ratio ≈ 2.3 on monolayer MoS₂. Corresponding SEM images are shown to the left, with scale bars corresponding to 20 nm. (b) and (c) show the simulated scattering and absorption spectra of the same bipyramids, respectively.

and

$$E_{vac} \propto \frac{1}{\sqrt{V}} \tag{4}$$

where N is the number of emitters coherently contributing to the interaction in the cavity, μ_e is the transition dipole moment of the quantum emitter, E_{vac} is the vacuum field and V is the mode volume of the resonator. This is defined as[54]

$$V = \frac{\int \varepsilon E^2 dV}{\text{Max}(\varepsilon E^2)} \tag{5}$$

where ε is the permittivity and E is the electric field strength.

Results and Discussion

The MoS₂ was grown in monolayer flakes by chemical vapour deposition (CVD) on a 300 nm SiO₂ layer on a Si substrate. CVD was chosen as the fabrication method due to its higher crystallinity and larger flake sizes in comparison with other methods.[55,56] The gold nano-bipyramids were synthesized from Au penta-twinned seeds[57,58] using a wet chemistry approach.[57] Cetyl trimethylammonium bromide (CTAB) was used as the stabilizing ligand. A high degree of control and uniformity of size and plasmon resonance energy was achieved within a batch of nano-bipyramids. Several batches of nano-bipyramids with different overall size, length, tip radius and aspect ratio were synthesized. The Au nano-bipyramids with a low concentration were drop-casted on MoS₂ flakes for single particle measurements. This allowed for in-depth investigation of the effect of the bipyramid's morphology on the strong coupling in the nano-bipyramid-MoS₂ system. All scattering spectra were measured under white light excitation at single particle level using a dark field microscope (see figure 1b). Each scattering spectrum was subsequently correlated with a scanning electron microscopy (SEM) image of the same nano-bipyramid, revealing the corresponding bipyramid's dimensions.

Prior to the bipyramid deposition, the MoS₂ flakes were characterized via Raman spectroscopy to ensure that they were monolayer (see figure 1c). The characteristic E' and A'₁ Raman peaks were observed to be 18.4 cm⁻¹ apart, confirming monolayer thickness of the flakes.[46,59–61] Figure 1d shows a typical photoluminescence (PL) spectrum of the monolayer flakes, later used in the scattering measurements. The large PL peak corresponds to the energy of the A exciton, matching the absorption of the A exciton in both energy position and width.[29] It can therefore be attributed to a direct-gap luminescence.[29] To achieve strong coupling, the plasmons of the Au nano-bipyramids were tuned to energetically overlap with the A exciton, i.e. the PL peak.

A slight blue shift of the PL peak was observed after the deposition of bipyramids onto the flakes, indicating a change in the exciton energy. The A exciton peak shifted from 1.82 eV to 1.88-1.90 eV. This effect has been previously reported in a similar system using WSe₂.[62] As in that case, it was found that the PL peak was slightly blue shifted, but the intensity and linewidth were not significantly affected. This observation excluded the hypothesis that the PL shift was due to trionic or defect-related emission.[62] In our simulations, a similar shift of the Rabi splitting dip to a new, higher energy was observed with the addition of a layer between the bipyramids and MoS₂ mimicking the CTAB-ligand.

Typical scattering spectra measured from a single bipyramid directly on the SiO₂/Si substrate and on a monolayer of MoS₂ are shown in figures 1e and 1f, respectively. Both bipyramids have the same dimensions of 95 nm × 40 nm. Insets show the corresponding SEM images. The longitudinal plasmon of the bipyramid on top of an MoS₂ flake is clearly seen to be split into two different eigenstates. The scattering for the polarization corresponding to the transverse mode was also measured. The scattering is much weaker and no peaks in the given energy range are evident in the transverse case. It is clear, therefore, that both observed peaks originate from the Rabi splitting due to the coupling of the longitudinal plasmon mode with the A exciton. The plasmon resonance energy of the Au bipyramids were tuned by adjusting their lengths and widths. A longer bipyramid or one with a higher aspect ratio has a lower energy plasmon resonance
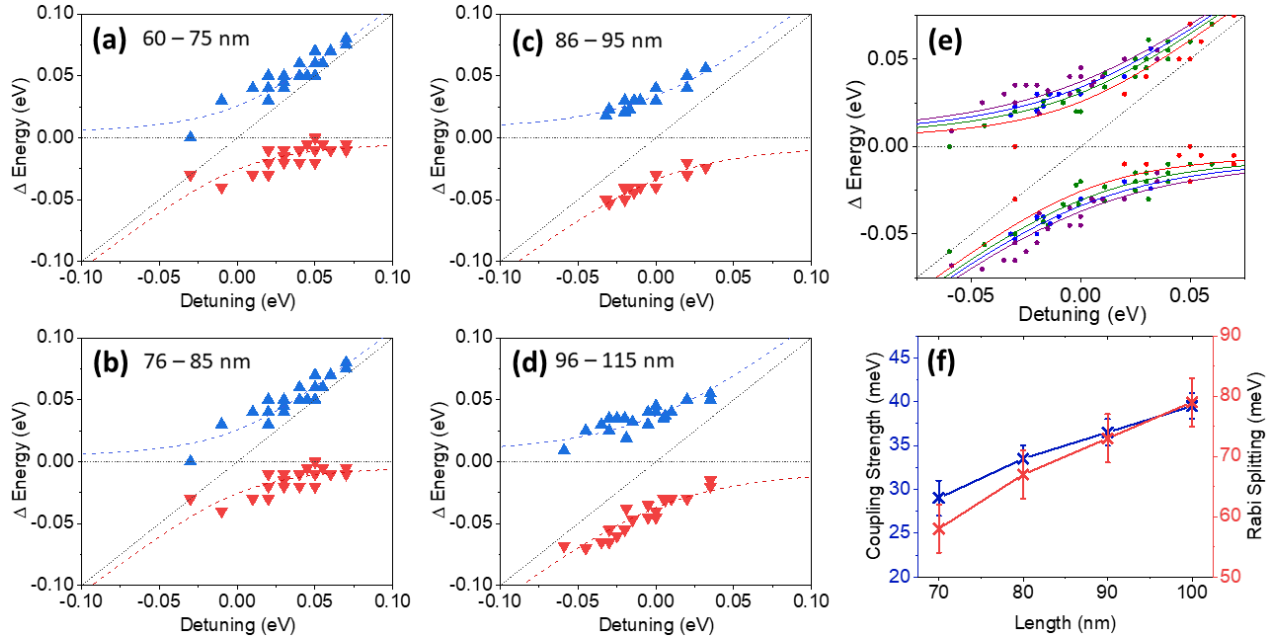
Figure 3. (a)-(d) Experimentally observed Rabi splitting using bipyramids of various sizes coupled to monolayer MoS_2. The plots show the difference in energy between the polaritons and the original plasmon plotted against the detuning of the original plasmon from the A exciton in MoS_2. The black horizontal and diagonal dashed lines show the energy of the A exciton in MoS_2 and plasmon energy of the bipyramids, respectively. The blue triangles show the energy of the upper polariton and the red triangles show the energy of the lower polariton. The dashed blue and red lines show the fit calculated from the coupled oscillator model (equation 1). (e) Rabi splitting plot of all data, with colours red, green, blue and purple showing the smallest to largest bipyramids, respectively. (f) Plot of coupling strength and Rabi splitting value at zero detuning for each size of bipyramids, estimated from the lines of best fit in plots a-d. The error bars indicate the range of values for coupling strength for which the average difference between the predicted and experimental energies of the polaritons is less than 2 meV. The corresponding Rabi splitting is then calculated from the coupling strength.

compared to a shorter bipyramid or one with a lower aspect ratio (see figure S1). The radius tip of the bipyramids was also seen to have an effect, blue shifting the plasmon resonance when it was increased. Sharper tips also produce stronger coupling between the plasmon and exciton in this system.

Figure 2 shows the scattering spectra of six different bipyramids coupled to a monolayer of MoS_2. The plasmon mode has been tuned from low to high energy through the A exciton PL energy. The bipyramids each have a similar aspect ratio of ≈ 2.3 and varying length between 70 and 110 nm. As previously discussed, the plasmon resonance of a bipyramid changes with bipyramid length, a larger bipyramid having a lower energy plasmon resonance. Figure 2a shows the experimental scattering spectrum for each of the bipyramids. The corresponding SEM images are shown to the left. As can be seen in the figure 2a, this has a large effect on the two polaritons. The longest bipyramid has the lowest energy plasmon resonance and gives larger scattering by the lower polariton when coupled to the MoS_2. It is seen that the shortest bipyramid has the highest plasmon resonance energy, and more light is scattered in the upper polariton in the coupled system.

Real strong coupling can be confused with Fano-like interferences when looking at scattering spectra.[17,63] Previous studies have found that only absorption measurements can be used to prove the presence of Rabi splitting.[15,17] An absence of splitting in the absorption would indicate that the effect seen in the scattering spectra is due to a Fano resonance.[15] Finite difference time domain (FDTD) simulations were carried out to reproduce the experimental scattering spectra (see figure 2b). In both the simulated and experimental data, the two polaritons are visible

with the dip in the middle occurring at the exciton energy. The simulations were also used to calculate the absorption spectra for each of the bipyramids (see figure 2c). This was to ensure that the peaks in the scattering spectra were not appearing due to interference. The absorption peaks were seen to have close resemblance to the scattering peaks, confirming that the observed effect is because of Rabi splitting.[15,17,63]

An extra peak is visible in the simulated spectra at about 2.05 eV. This peak arises due to the presence of the B exciton (see figure S2). The B exciton is not seen to have as visible an effect in the experimental spectra. The simulated spectra are seen to have slightly broader peaks than in the experimental data. The dielectric function used for the simulations[64] can differ slightly from the experimental MoS_2. Altering the dielectric function to have higher amplitude for the excitonic peaks would narrow the simulated the polariton peaks. Therefore, the slightly broader simulation spectral peaks are attributed to a small discrepancy of the dielectric function, which is a close approximation to the experimental MoS_2

Separate anti-crossing plots were made using the experimental data for the different sized bipyramids. The size categories studied were those of bipyramids with length between 60-75 nm, 76-85 nm, 86-95 nm and 96-115 nm, shown in figure 3a-d. Each size category included bipyramids on several different samples, ensuring that any trends found in the plots were due to the different bipyramid sizes. The bipyramids studied had varying aspect ratios, allowing for a range of plasmon energies to be studied for each size. The polariton energies are shown as the difference in energy, $\Delta Energy$, of the scattering peaks from the A exciton in MoS_2. This accounts for slight differences (0.02 eV)
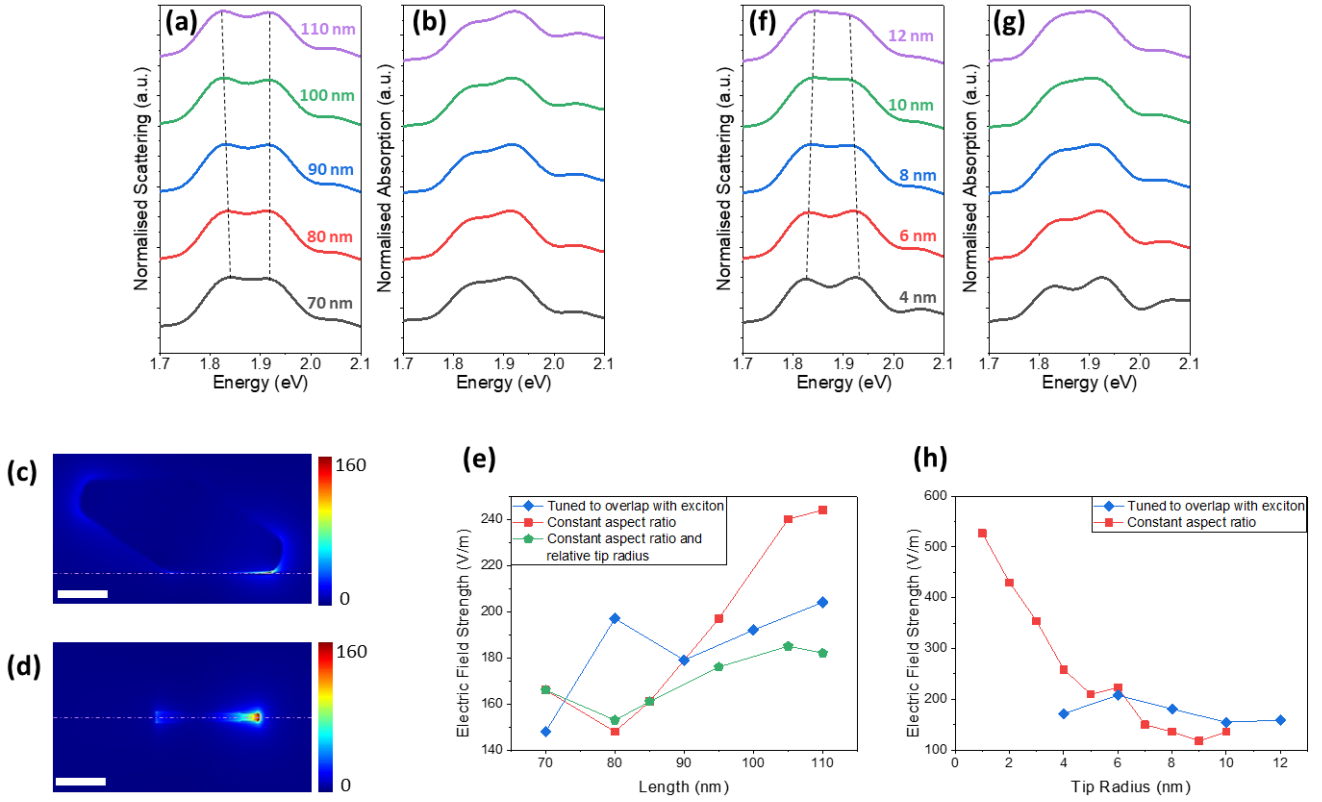
Figure 4. (a) and (b) Simulated scattering and absorption spectra of bipyramids, coupled to MoS₂, of length 70-110 nm and fixed tip radius of 7 nm, with adjusted aspect ratios to ensure zero detuning between the plasmon and exciton. (c) and (d) Typical local electric field strength maps, perpendicular to each other, (in V/m) of the cross section through the middle of the bipyramid and against the substrate where the bipyramid is resting respectively. The purple dashed line in figure c shows the position of the perpendicular slice shown in figure d and vice versa. They are taken at the energy of highest electric field strength (energy of the exciton) White scale bars show 20 nm.(e) Plot of the electric field strength (V/m) at the tip of different bipyramids with varying length between 70-110 nm. The blue graph corresponds to the bipyramids presented in (a) and (b), the red curve corresponds to bipyramids with a fixed aspect ratio and fixed tip radius of 7 nm and the green curve corresponds to bipyramids with a fixed tip radius to width ratio and aspect ratio. (f) and (g) Simulated scattering and absorption spectra of bipyramids with varying tip radii between 4-12 nm and fixed length 80 nm. The aspect ratios were adjusted to ensure zero detuning between the plasmon and exciton. (h) Plot of the electric field (V/m) at the tip of bipyramids of tip radius 2-12 nm corresponding to the bipyramids presented in (c) and (d) (blue) and to bipyramids of fixed length and aspect ratio (red).

in exciton energy between samples. The A exciton energy in the MoS₂ was taken as the energy position of the strongest peak in the measured PL spectrum (figure 1c). $\Delta Energy$ is plotted against the energy detuning of the plasmon from the A exciton in the MoS₂. Clear anti-crossing behaviour is seen in each plot, the upper and lower polaritons having higher and lower energy than the original plasmon and exciton.

A coupled oscillator model was used to fit the data obtained from the dark field scattering measurements, using equation 1. The method of using the coupled oscillator model to extract coupling strength and Rabi splitting values from experimentally measured data is commonly used for open cavity systems.[14,18,43,65–67] The energies of the upper and lower polaritons were taken as the highest points in intensity in the centre of the polariton peaks. According to Savona *et al*., the polaritons measured will have peaks at different values depending on the method used. The simulation data showed that the difference in the splitting between the scattering and absorption spectra was 7 ± 4% of the total splitting calculated from the scattering spectrum. The splitting observed in the scattering spectra is always slightly higher than that from the absorption spectra. This is a

small difference and shows that the coupled oscillator model can be used to estimate g with a margin of error of ~10%.

The dissipation rates of the plasmons were estimated by averaging the full-width-half-maxima (FWHM) of the single particle scattering measurements on an SiO₂/Si substrate (figure 1d). This allows for the dissipation rate of the plasmon uncoupled to MoS₂ to be obtained. The γ_{pl} was constant for all particle sizes studied. This was confirmed with FDTD simulations. The average linewidth at FWHM for all particles measured on a SiO₂/Si substrate was found to be ~ 105 meV. The dissipation rate of the exciton was taken by averaging the FWHM of the PL measurements of the MoS₂ flakes (figure 1e). It was found to be ~ 50 meV. The uncoupled plasmon energy was estimated from the spectral data using[14]:

$$\omega_{pl} = \omega_{up} + \omega_{lp} - \omega_{ex} \qquad (6)$$

The coupling constant, g, was estimated by fitting with equation 1. This was done by finding a g such that the average difference in predicted and measured polariton energies was less than 2 meV within the sample of bipyramids. (The predicted value of polariton energy for a given g was found using equation 1.)

The dashed curved lines on the plots show the fitted upper (blue) and lower (red) polaritons, respectively, for the estimated g. The dashed horizontal and diagonal lines indicate the positions of the exciton and plasmon, respectively.

Figure 3e shows the results for bipyramids within each size category plotted together. Each size of bipyramids is given a different colour, indicating the clear trend of larger bipyramids having a stronger coupling constant. Figure 3f shows the trend of the coupling constant, g, increasing with bipyramid size. The coupling constant for each plot was found from the best fit with the experimental data. The Rabi splitting separation at zero detuning, Ω, was also estimated from the coupling constant, using equation:[13,47]

$$\Omega = \sqrt{4g^2 - \frac{(\Delta\gamma)^2}{4}} \qquad (7)$$

Evidence for increased splitting for larger bipyramids can also be seen in figure 2; the distance between the two polaritons is visibly greater for the larger bipyramids. Figure 3e shows that the Rabi splitting increases from ~55 meV for 70 nm long bipyramids to ~80 meV for 100 nm bipyramids. These values agree with those from the experimental scattering spectra (see figure S3).

Several reports indicate various criteria to achieve strong coupling including $\mathbf{g} > \gamma_{pl}, \gamma_{ex}$,[17,48,50] $\mathbf{g} > \sqrt{\gamma_{pl}\gamma_{ex}}$,[17] and $\Omega > \frac{\gamma_{pl}+\gamma_{ex}}{2}$.[14,48,49] In our work, Ω ranges between 50 and 80 meV, and γ_{pl} and γ_{ex} are 105 meV and 50 meV, respectively. Only the bipyramids > 90 nm in length meet the criteria for Ω, and the system does not meet the requirements for the other criteria mentioned due to the broad linewidth of the plasmon resonance. However, other evidence suggests strong coupling is occurring for all bipyramid sizes. The FWHM across the two visible peaks was measured from the scattering spectra of bipyramids of all sizes on a monolayer of MoS_2 with $\sim$ zero detuning between the plasmon and exciton. The average of these was found to be ~ 150 meV which is significantly larger than that found for bipyramids on the SiO_2/Si substrate (~ 105 mev). This indicates that more than an interference effect is taking place, the two separate peaks being spaced further apart. This broadening effect is visible in figures 1e and f. The absorption spectra in figures 2 and 4 also support that Rabi splitting is occurring for these sizes of bipyramids. It is also clear, however, that the 70 nm bipyramids are on the edge of to the weak coupling regime. $\Omega \sim 50$ meV (near γ_{ex}), and the absorption spectra show the two peaks nearing each other in figure 4 for that size category.

The result of the coupling strength increasing with increased metal volume is in contrast with previous findings for different shaped nanoresonators.[16,17] As the length of a bipyramid is increased, the volume generally also increases. In the case of the bipyramids in this study, the aspect ratio must be reduced for bipyramids of longer lengths to keep the plasmon resonance at the same energy, which further increases the volume. Therefore, the metal volume of a bipyramid with a given plasmon energy increases with length. Further simulations of the electric field elucidate the observed size dependence of the Rabi splitting. Figure 4a and b show the dependence of the coupling strength on the overall volume of the bipyramid. The length was varied within the range of the experimental data, from 70 nm to 110 nm. The aspect ratio was varied to keep the zero-detuning condition between the plasmon and exciton. The overall volume was varied between 25,000 nm^3 and 110,000 nm^3. The tip radius was kept constant at 7 nm for each bipyramid size. Figure 4a and b show the simulated scattering and absorption. The coupling strength is seen to increase by ~ 20 meV across the volume range, in agreement with the experimental data in figure 3.

A typical distribution of the electric field strength (V/m) in the cross section through the centre of the bipyramid is shown in figure 4c. The electric field strength of the system was calculated using FDTD simulations. Figure 4d shows a map (perpendicular to the that in Figure 4c) of electric field strength (V/m) within the MoS_2 layer where the plasmon is interacting with the exciton. Both maps are shown where the field strength is highest, at the energy of the A exciton. These electric field maps are for the 85 nm bipyramid in figure 2 (2.3 aspect ratio and 7 nm tip radius). It is clear that the electric field is enhanced and localised at the tips interacting with the MoS_2. Figure 4e (blue) shows the corresponding electric field strength at the tips of the bipyramids, with spectra presented in figures 4 a and b. The steady upward trend mirrors the increased Rabi splitting for the larger bipyramids. There is an unexpected rise in the electric field for the bipyramid with 80 nm length. This can be attributed to the change in aspect ratio necessary to keep all the bipyramid plasmons energetically coincident with the exciton in MoS_2. The aspect ratio must be reduced for the longer bipyramids, causing a blunting effect on the tips and lower electric field density.

The simulated electric fields at the tips of the bipyramids from figure 2 were also investigated (see red line in figure 4e). The lengths of these bipyramids also varied from 70-110 nm, and had a 7 nm tip radius, but this time had a constant aspect ratio of 2.3. Here, there is a steady increase in the electric field. (The highest electric field strength for the 70 nm bipyramid is at 636 nm, not overlapping with the exciton energy as is true of the other bipyramids investigated. This explains why the E field strength is slightly higher than expected for this simulation.) A possible reason for the increase of electric field strength with bipyramid length is that the larger bipyramids are closer to the ideal bipyramid shape. This is because, experimentally, there is a limit to how sharp the bipyramid tips can be. Thermodynamically, it would not be possible for them to be less than a few nanometers.[68] Therefore, for the smaller bipyramids, the tip would be a more significant proportion of the overall width of the bipyramid, making it more rod-like. A third simulation was carried out to investigate this (see figure 4e green line). In the simulation, the ratio of the tip radius to overall bipyramid width was kept constant. The aspect ratio was again fixed at 2.3. The proportions of the 85 nm bipyramid from figure 2 were chosen. A steady increase in electric field is observed, but less than what was found by keeping the tip radius fixed. The radius is eventually large enough for the 110 nm case for the field strength to decrease. The smallest bipyramid exhibits a larger electric field strength than might be expected. This is due to the very sharp tips required to keep the same proportions as the other bipyramids, significantly reducing the resonance mode volume. This result suggests that the ratio of overall width to tip is not the only factor influencing the increased field in the tips of the larger bipyramids. The plasmon within the larger bipyramids is stronger due to the extra electrons present in the larger metal volume. The field enhancement, however, is still concentrated at the same equally sharp tips, resulting in a stronger coupling for the larger bipyramids. This would also explain why the opposite effect was seen in the study by Antosiewicz et al.,[17] in which case the simulations considered spheres, without sharp tips to further concentrate the electric field.

For larger bipyramids, the mode volume is seen to increase slightly, due to a stronger plasmon resonance. This trend is visible in figure S4. The mode volume is determined using equation 5. The field is calculated using FDTD simulations and integrated over the volume of the MoS$_2$ underneath the bipyramid. However, the larger bipyramids used in this study have equally sharp tips as the small ones, and the aspect ratio of the larger bipyramids is reduced in order to have the plasmon resonance at the same energy as the A exciton of MoS$_2$. Both of these factors allow for the electric field to be aligned more directly into the surface (and therefore into the MoS$_2$) when the bipyramid is larger. This effect is further elucidated in the schematic in figure S5. This direct alignment focuses the E field into the MoS$_2$, concentrating it into a smaller mode volume. A large aspect ratio or large tip radius results in the electric field overlapping the MoS$_2$ at a more oblique angle. This causes the electric field to overlap less strongly and with a larger area of MoS$_2$, increasing the mode volume. This effect can be seen in figure S4, as the mode volume is shown to decrease when the bipyramid reaches ~ 90 nm in length when the bipyramids are tuned to overlap the A exciton. When a constant aspect ratio is kept, a similar trend is seen, due to the tip radius being kept constant (so lower in proportion to the rest of the bipyramid). The rise in mode volume with bipyramid length is only seen consistently when the aspect ratio and tip radius are adjusted with the length to keep the proportions of the bipyramid the same. When the length is kept constant, but the tip radius is increased, a clear trend of increased mode volume is seen, even when the aspect ratio is reduced to overlap the plasmon with the A exciton, as is seen in figure S4(b).

Figure S6 elucidates how the mode volume changes outside the MoS$_2$ layer. The mode volume at the tip increases for longer bipyramids, but only very slightly. The difference is more significant when the tip radius is increased, with the mode volume larger for bipyramids with larger tip radii.

The importance of the sharpness of the tips was also investigated, as shown in figure 4f and g. The length of each bipyramid was kept constant, at 80 nm. As in the previous example, the aspect ratio was adjusted slightly for each simulation to maintain zero-detuning between the plasmon and exciton. The aspect ratio was increased for the bipyramids with larger tips to prevent the plasmon from blue shifting. A clear trend is visible as the tip radius was increased from 4 nm to 12 nm as the splitting decreases by 35 meV. There are two reasons for this difference. As the tip gets less sharp, the nanoparticle gets more rod-like, causing the resonance to spectrally broaden, increasing γ_{pl}, the plasmon line width. According to equation 2, when γ_{pl} gets too big, the system transitions to the weak coupling regime. This is visible in the absorption spectra (figure 4g) as the tip is increased past 10 nm, the two polaritons are no longer distinguishable from each other. Another factor contributing to this effect is the increased mode volume of the resonator with increased tip radius. This also reduces the coupling strength, according to equations 3 and 4. A decrease in electric field is observed for larger tips, as expected (see figure 4h, blue line). It is slightly lower than expected for the 4 nm tip radius, attributed to the low aspect ratio required to blue-shift the plasmon to the correct energy. The results emphasize the importance of sharp tips to achieve larger splitting between the polaritons.

In the case where the aspect ratio is fixed while the tip radius changes from 1 nm to 10 nm (see figure 4h, red line), the results are as expected. The field decreases with a larger tip radius and gets very large when the radius is reduced to unfeasibly small sizes. The field for the 6 nm tip radius is higher than expected. Upon further investigation, it was observed that this is the bipyramid with closest to zero detuning between its plasmon and the exciton. It therefore has the strongest interaction with the MoS$_2$, resulting in a slightly larger electric field.

Figures 4e and h show some bipyramids with the highest electric field strength being at a different energy to that of the A exciton. These are the 70 nm long bipyramid in figure 4e (red line) and the bipyramids of tip radii 1,2,3,4,5 and 10 in figure 4h (red line). The highest electric field strength for each of these bipyramids is higher than it would be if it were more strongly coupled to the MoS$_2$ layer (but the peak of high intensity has a lower FWHM). This effect is visible in figures 4e and h.

The electric field strength directly under the bipyramid's tip within the CTAB-mimicking layer and MoS$_2$ layer was also investigated (see figure S7). This was to show how the modal field's overlap with the ultrathin MoS$_2$ layer depends on the bipyramid length and tip radius. The average electric field strength within these layers was shown to increase as the bipyramid length increased or the tip radius decreased. Further, the electric field strength was shown to penetrate further through the CTAB layer and into the substrate, hence resulting in stronger interaction with the MoS$_2$ monolayer, for longer lengths and smaller tip radii. This gives further evidence as to how larger bipyramids with sharp tips produce stronger coupling in this system.

Conclusions

In conclusion, we have investigated the dependence of Rabi splitting on bipyramid shape and dimensions. It is shown that the coupling strength is strongly influenced by the both tip radius and the length of the bipyramid being used. The tip sharpness plays a crucial role, with a transition to the weak coupling regime if not sharp enough. To benefit from the largest field enhancements and the largest Rabi splitting, for a bipyramid with a fixed aspect ratio, very sharp tips with radii of less than 7 nm are required. The dependence of the field strength on the bipyramid length has also been clearly observed. The localization of the field enhancement at the tips makes larger bipyramids preferable to achieve strong coupling. Rabi splitting is observed to increase from ~55 meV with a 70 nm long bipyramid to ~ 80 meV for a 100 nm long bipyramid. We have shown how the coupling strength in a Rabi splitting system can be enhanced by increasing the metal volume of the nanoantennae. This has not been achieved before without also increasing the number of excitons coupled into the system. This study has shown that the shape of the nanoresonator must be carefully considered when choosing the ideal size of nanoparticle to achieve strong coupling.

Methods

Growth of MoS$_2$: Monolayer MoS$_2$ flakes were grown by chemical vapour deposition (CVD) on a 300 nm SiO$_2$ layer on a Si substrate. A target substrate (SiO$_2$/Si) was placed face-down on a seed substrate (liquid-phase exfoliated MoO$_3$ nanosheets drop cast onto a 300 nm layer of SiO$_2$ on Si[69]). This formed a microreactor which was placed in the centre of a quartz tube furnace. It was heated to 750 °C under 150 standard cubic centimetres per minute (sccm) Ar flow at a pressure of ~0.7 Torr. Sulfur

vapour was generated by heating sulfur powder to ≈ 120 °C in a separate downstream part of the furnace. The microreactor was exposed to the sulfur vapour for the growth of monolayer MoS_2 flakes, with forming gas as a carrier.[56]

Photolithography: Photolithography was carried out so the dark field spectra of individual gold bipyramids could be correlated with their corresponding SEM images. It was done with an OAI mask aligner. The photoresist and photodeveloper used were S1813 resist and MF-319 developer respectively. The metal used was a 5 nm adhesion layer of Ti and 35 nm Au. NMP 1165 developer, acetone and isopropyl alcohol were used to etch away the metal.

Bipyramid Synthesis: Au penta-twinned seeds were synthesised.[57] A 10 mL solution containing 0.125 mM $HAuCl_4$ and 0.25 mM sodium citrate was prepared. 0.15 mL of 10 mM $NaBH_4$ was added. This changed the solution from colourless to slightly pink. The seeds were aged for two hours before use. The solution to grow the bipyramids out of seeds was prepared[57] using a 0.1 M cetyl trimethylammonium bromide (CTAB) solution. 0.5 mL of a 10 mM $HAuCl_4$ and 0.1 mL 10 mM $AgNO_3$ were added. 0.2 mL of 1.0 M HCl was added to acidify the solution. 0.08mL of 0.1 M ascorbic acid was added to reduce the Au(III) to Au(I). 80 μL of seeds were added to the solution. The reaction was carried out in a 30 °C water bath for two hours, until the solution turned purple. The concentration of the seeds and $HAuCl_4$ solution were varied to change the overall volume of the bipyramids. The concentrations of the ascorbic acid and $AgNO_3$ solutions were varied to alter the aspect ratios. The bipyramids were diluted in ethanol before dropping onto the CVD-grown MoS_2. All chemicals were purchased from Sigma Aldrich.

MoS_2 Characterisation: The MoS_2 was excited with a 532 nm laser. The photoluminescence spectra were recorded with an Andor 230i spectrometer. The Raman spectra were recorded with a Horiba Jobin Yvon Raman spectrometer. A $100\times$ objective was used for both sets of measurements.

Dark-Field Measurements: The dark field measurements were taken with a dark field microscope and a $100\times$ objective. The measurements were taken with an Andor CCD camera and an Andor 230i spectrometer.

Scanning Electron Microscopy: The SEM images were taken with a Zeiss Ultra scanning electron microscope, operating at 5 kV. Measurements were made using the InLens detector. Adhesive electrically conductive paint, silver loaded form RS Pro was used as a conductive layer.

Numerical Simulations: The finite-difference-time-domain method with FDTD solutions, Lumerical, was used. This was used to calculate the scattering, absorption, electric field strength and modal volume of the system. The dimensions of the bipyramids were taken from the corresponding SEM images. The bipyramids were approximated as two cones connected at their base (allowing for the rounding effect seen in nature with particles that size). See figure S8. The bipyramid is placed on a substrate as in experiments – 0.5 nm CTAB-mimicking layer (with an refractive index of n=1.45[70]), 0.75 nm thick of monolayer MoS_2, 300 nm layer thick SiO_2 and 1 mm layer Si. The thickness of the CTAB layer was chosen as it most closely resembled the experimental data. The permittivity of monolayer MoS_2 and Au is taken from Jung et al.[64] and Johnson and Christy[71] respectively. The TMDC was modelled as an isotropic material. The bipyramid is meshed with 1 nm resolution, with 0.5 nm resolution at the tips and 0.375 nm and 0.2 nm

resolution along the thickness of the MoS_2 layer and CTAB layer respectively.

ASSOCIATED CONTENT

Supporting Information

Examples of experimental scattering of single bipyramids on the SiO_2/Si substrate for varying sizes and aspect ratios, simulated dependence of the scattering and absorption spectra on the A and B exciton of MoS_2, examples of experimental scattering of bipyramids of various sizes coupled to a monolayer of MoS_2 at zero detuning, simulated mode volume dependence on bipyramid length and tip radius, explanation of mode volume dependence on bipyramid length and tip radius, electric field dependence on bipyramid length and tip radius, simulated average electric field strength within the MoS_2 and CTAB-mimicking layer and as a ratio of MoS_2 to the CTAB-mimicking layer for bipyramids of various lengths and tip radii, comparison of simulated scattering spectra of bipyramids modelled with two cones and bipyramids modelled with ten sides.

This material is available free of charge via the Internet at http://pubs.acs.org.

AUTHOR INFORMATION

Corresponding Author

* Email: bradlel@tcd.ie

Author Contributions

All authors have given approval to the final version of the manuscript.

Notes

The authors declare no competing financial interest.

ORCID

Julia Lawless: 0000-0003-1472-2218

Calin Hrelescu: 0000-0002-2410-4512

Carolyn Elliott: 0000-0002-9197-8906

Lisanne Peters: 0000-0002-0551-6263

Niall McEvoy: 0000-0001-5950-8755

A. Louise Bradley: 0000-0002-9399-8628

REFERENCES

(1)   Purcell, E. M. Spontaneous Emission Probabilities at Radio Frequencies. *Phys. Rev.* **1946**, *69*, 681. https://doi.org/10.1007/978-1-4615-1963-8_40.

(2)   Cao, E.; Lin, W.; Sun, M.; Liang, W.; Song, Y. Exciton-Plasmon Coupling Interactions: From Principle to Applications. *Nanophotonics* **2018**, *7* (1), 145–167. https://doi.org/10.1515/nanoph-2017-0059.

(3)   Thomas, A.; George, J.; Shalabney, A.; Dryzhakov, M.; Varma, S. J.; Moran, J.; Chervy, T.; Zhong, X.; Devaux, E.; Genet, C. et al. Ground-State Chemical Reactivity under Vibrational Coupling to the Vacuum Electromagnetic Field. *Angew. Chemie* **2016**, *128* (38), 11634–11638. https://doi.org/10.1002/ange.201605504.

(4)   Pang, Y.; Thomas, A.; Nagarajan, K.; Vergauwe, R. M. A.; Joseph, K.; Patrahau, B.; Wang, K.; Genet, C.; Ebbesen, T. W. On the Role of Symmetry in Vibrational Strong Coupling: The Case of Charge-Transfer Complexation. *Angew. Chemie - Int. Ed.* **2020**, *59* (26). https://doi.org/10.1002/anie.202002527.

(5)   Thomas, A.; Jayachandran, A.; Lethuillier-Karl, L.; Vergauwe, R. M. A.; Nagarajan, K.; Devaux, E.; Genet, C.; Moran, J.; Ebbesen, T. W. Ground State Chemistry under Vibrational Strong Coupling: Dependence of Thermodynamic Parameters on the Rabi Splitting Energy. *Nanophotonics* **2020**, *9* (2), 249–255. https://doi.org/10.1515/nanoph-2019-0340.

(6)   Noda, S.; Fujita, M.; Asano, T. Spontaneous-Emission Control by Photonic Crystals and Nanocavities. *Nat. Photonics* **2007**, *1* (8), 449. https://doi.org/10.1038/nphoton.2007.141.

(7)   Vasa, P.; Pomraenke, R.; Cirmi, G.; De Re, E.; Wang, W.; Schwieger, S.; Leipold, D.; Runge, E.; Cerullo, G.; Lienau, C. Ultrafast Manipulation of Strong Coupling in Metal-Molecular Aggregate Hybrid Nanostructures. *ACS Nano* **2010**, *4* (12), 7559–7565. https://doi.org/10.1021/nn101973p.

(8)   Imamoglu, A.; Awschalom, D. D.; Burkard, G.; DiVincenzo, D. P.; Loss, D.; Sherwin, M.; Small, A. Quantum Information Processing Using Quantum Dot Spins and Cavity Qed. *Phys. Rev. Lett.* **1999**, *83* (20), 4204. https://doi.org/10.1103/PhysRevLett.83.4204.

(9)   Reithmaier, J. P.; Sęk, G.; Löffler, A.; Hofmann, C.; Kuhn, S.; Reitzenstein, S.; Keldysh, L. V.; Kulakovskii, V. D.; Reinecke, T. L.; Forchel, A. Strong Coupling in a Single Quantum Dot-Semiconductor Microcavity System. *Nature* **2004**, *432* (7014), 197–200. https://doi.org/10.1038/nature02969.

(10)   Yoshle, T.; Scherer, A.; Hendrickson, J.; Khitrova, G.; Gibbs, H. M.; Rupper, G.; Ell, C.; Shchekin, O. B.; Deppe, D. G. Vacuum Rabi Splitting with a Single Quantum Dot in a Photonic Crystal Nanocavity. *Nature* **2004**, *432* (7014), 200–203. https://doi.org/10.1038/nature03119.

(11)   Milde, F.; Knorr, A.; Hughes, S. Role of Electron-Phonon Scattering on the Vacuum Rabi Splitting of a Single-Quantum Dot and a Photonic Crystal Nanocavity. *Phys. Rev. B - Condens. Matter Mater. Phys.* **2008**, *78* (3), 035330. https://doi.org/10.1103/PhysRevB.78.035330.

(12)   Peter, E.; Senellart, P.; Martrou, D.; Lemaître, A.; Hours, J.; Gérard, J. M.; Bloch, J. Exciton-Photon Strong-Coupling Regime for a Single Quantum Dot Embedded in a Microcavity. *Phys. Rev. Lett.* **2005**, *95* (6), 067401. https://doi.org/10.1103/PhysRevLett.95.067401.

(13)   Törmä, P.; Barnes, W. L. Strong Coupling between Surface Plasmon Polaritons and Emitters. *Rep. Prog. Phys.* **2015**, *78* (1), 013901. https://doi.org/10.1088/0034-4885/78/1/013901.

(14)   Stührenberg, M.; Munkhbat, B.; Baranov, D. G.; Cuadra, J.; Yankovich, A. B.; Antosiewicz, T. J.; Olsson, E.; Shegai, T. Strong Light-Matter Coupling between Plasmons in Individual Gold Bi-Pyramids and Excitons in Mono- and Multilayer WSe$_2$. *Nano Lett.* **2018**, *18* (9), 5938–5945. https://doi.org/10.1021/acs.nanolett.8b02652.

(15)   Stete, F.; Koopman, W.; Bargheer, M. Signatures of Strong Coupling on Nanoparticles: Revealing Absorption Anticrossing by Tuning the Dielectric Environment. *ACS Photonics* **2017**, *4* (7), 1669–1676. https://doi.org/10.1021/acsphotonics.7b00113.

(16)   Munkhbat, B.; Baranov, D. G.; Bisht, A.; Hoque, M. A.; Karpiak, B.; Dash, S. P.; Shegai, T. Electrical Control of Hybrid Monolayer Tungsten Disulfide–Plasmonic Nanoantenna Light–Matter States at Cryogenic and Room Temperatures. *ACS Nano* **2020**, *14* (1), 1196–1206.

https://doi.org/10.1021/acsnano.9b09684.

(17)   Antosiewicz, T. J.; Apell, S. P.; Shegai, T. Plasmon-Exciton Interactions in a Core-Shell Geometry: From Enhanced Absorption to Strong Coupling. *ACS Photonics* **2014**, *1* (5), 454–463. https://doi.org/10.1021/ph500032d.

(18)   Zhang, L.; Gogna, R.; Burg, W.; Tutuc, E.; Deng, H. Photonic-Crystal Exciton-Polaritons in Monolayer Semiconductors. *Nat. Commun.* **2018**, *9* (1), 1–8. https://doi.org/10.1038/s41467-018-03188-x.

(19)   Balci, S. Ultrastrong Plasmon–Exciton Coupling in Metal Nanoprisms with J-Aggregates. *Opt. Lett.* **2013**, *38* (21), 4498. https://doi.org/10.1364/ol.38.004498.

(20)   Schlather, A. E.; Large, N.; Urban, A. S.; Nordlander, P.; Halas, N. J. Near-Field Mediated Plexcitonic Coupling and Giant Rabi Splitting in Individual Metallic Dimers. *Nano Lett.* **2013**, *13* (7), 3281–3286. https://doi.org/10.1021/nl4014887.

(21)   Wersall, M.; Cuadra, J.; Antosiewicz, T. J.; Balci, S.; Shegai, T. Observation of Mode Splitting in Photoluminescence of Individual Plasmonic Nanoparticles Strongly Coupled to Molecular Excitons. *Nano Lett.* **2017**, *17* (1), 551–558. https://doi.org/10.1021/acs.nanolett.6b04659.

(22)   Lepeshov, S.; Wang, M.; Krasnok, A.; Kotov, O.; Zhang, T.; Liu, H.; Jiang, T.; Korgel, B.; Terrones, M.; Zheng, Y. et al. Tunable Resonance Coupling in Single Si Nanoparticle-Monolayer WS$_2$ Structures. *ACS Appl. Mater. Interfaces* **2018**, *10* (19), 16690–16697. https://doi.org/10.1021/acsami.7b17112.

(23)   Bisht, A.; Cuadra, J.; Wersäll, M.; Canales, A.; Antosiewicz, T. J.; Shegai, T. Collective Strong Light-Matter Coupling in Hierarchical Microcavity-Plasmon-Exciton Systems. *Nano Lett.* **2019**, *19* (1), 189–196. https://doi.org/10.1021/acs.nanolett.8b03639.

(24)   Liu, L.; Tobing, L. Y. M.; Yu, X.; Tong, J.; Qiang, B.; Fernández-Domínguez, A. I.; Garcia-Vidal, F. J.; Zhang, D. H.; Wang, Q. J.; Luo, Y. Strong Plasmon–Exciton Interactions on Nanoantenna Array–Monolayer WS 2 Hybrid System. *Adv. Opt. Mater.* **2019**, 1901002. https://doi.org/10.1002/adom.201901002.

(25)   Han, X.; Wang, K.; Xing, X.; Wang, M.; Lu, P. Rabi Splitting in a Plasmonic Nanocavity Coupled to a WS$_2$ Monolayer at Room Temperature. *ACS Photonics* **2018**, *5* (10), 3970–3976. https://doi.org/10.1021/acsphotonics.8b00931.

(26)   Wang, S.; Le-Van, Q.; Vaianella, F.; Maes, B.; Eizagirre Barker, S.; Godiksen, R. H.; Curto, A. G.; Gomez Rivas, J. Limits to Strong Coupling of Excitons in Multilayer WS 2 with Collective Plasmonic Resonances. *ACS Photonics* **2019**, *6* (2), 286–293. https://doi.org/10.1021/acsphotonics.8b01459.

(27)   Geisler, M.; Cui, X.; Wang, J.; Rindzevicius, T.; Gammelgaard, L.; Jessen, B. S.; Gonçalves, P. A. D.; Todisco, F.; Bøggild, P.; Boisen, A. et al. Single-Crystalline Gold Nanodisks on WS 2 Mono- and Multilayers for Strong Coupling at Room Temperature. *ACS Photonics* **2019**, *6* (4), 994–1001. https://doi.org/10.1021/acsphotonics.8b01766.

(28)   Kleemann, M. E.; Chikkaraddy, R.; Alexeev, E. M.; Kos, D.; Carnegie, C.; Deacon, W.; De Pury, A. C.; Große, C.; De Nijs, B.; Mertens, J. et al. Strong-Coupling of WSe$_2$ in Ultra-Compact Plasmonic Nanocavities at Room Temperature. *Nat. Commun.* **2017**, *8* (1), 1–7. https://doi.org/10.1038/s41467-017-01398-3.

(29)   Mak, K. F.; Lee, C.; Hone, J.; Shan, J.; Heinz, T. F. Atomically Thin MoS$_2$: A New Direct-Gap Semiconductor. *Phys. Rev. Lett.* **2010**, *105* (13), 136805. https://doi.org/10.1103/PhysRevLett.105.136805.

(30)   Kang, J.; Seo, J. W. T.; Alducin, D.; Ponce, A.; Yacaman, M. J.; Hersam, M. C. Thickness Sorting of Two-Dimensional Transition Metal Dichalcogenides via Copolymer-Assisted Density Gradient Ultracentrifugation. *Nat. Commun.* **2014**, *5*, 5478. https://doi.org/10.1038/ncomms6478.

(31)   Duan, X.; Wang, C.; Pan, A.; Yu, R.; Duan, X. Two-Dimensional Transition Metal Dichalcogenides as Atomically Thin Semiconductors: Opportunities and Challenges. *Chem. Soc. Rev.* **2015**, *44* (24), 8859–8876. https://doi.org/10.1039/c5cs00507h.

(32)   Mak, K. F.; Shan, J. Photonics and Optoelectronics of 2D Semiconductor Transition Metal Dichalcogenides. *Nat. Photonics* **2016**, *10* (4), 216.

https://doi.org/10.1038/nphoton.2015.282.

(33) Lebègue, S.; Eriksson, O. Electronic Structure of Two-Dimensional Crystals from Ab Initio Theory. *Phys. Rev. B - Condens. Matter Mater. Phys.* **2009**, *79* (11), 115409. https://doi.org/10.1103/PhysRevB.79.115409.

(34) Kuc, A.; Zibouche, N.; Heine, T. Influence of Quantum Confinement on the Electronic Structure of the Transition Metal Sulfide TS2. *Phys. Rev. B - Condens. Matter Mater. Phys.* **2011**, *83* (24), 245213. https://doi.org/10.1103/PhysRevB.83.245213.

(35) Cheiwchanchamnangij, T.; Lambrecht, W. R. L. Quasiparticle Band Structure Calculation of Monolayer, Bilayer, and Bulk MoS 2. *Phys. Rev. B - Condens. Matter Mater. Phys.* **2012**, *85* (20), 205302. https://doi.org/10.1103/PhysRevB.85.205302.

(36) Zeng, H.; Liu, G. Bin; Dai, J.; Yan, Y.; Zhu, B.; He, R.; Xie, L.; Xu, S.; Chen, X.; Yao, W. et al. Optical Signature of Symmetry Variations and Spin-Valley Coupling in Atomically Thin Tungsten Dichalcogenides. *Sci. Rep.* **2013**, *3*, 1608. https://doi.org/10.1038/srep01608.

(37) Lee, B.; Liu, W.; Naylor, C. H.; Park, J.; Malek, S. C.; Berger, J. S.; Johnson, A. T. C.; Agarwal, R. Electrical Tuning of Exciton-Plasmon Polariton Coupling in Monolayer MoS$_2$ Integrated with Plasmonic Nanoantenna Lattice. *Nano Lett.* **2017**, *17* (7), 4541–4547. https://doi.org/10.1021/acs.nanolett.7b02245.

(38) Baranov, D. G.; Wersäll, M.; Cuadra, J.; Antosiewicz, T. J.; Shegai, T. Novel Nanostructures and Materials for Strong Light-Matter Interactions. *ACS Photonics* **2018**, *5* (1), 24–42. https://doi.org/10.1021/acsphotonics.7b00674.

(39) Dufferwiel, S.; Schwarz, S.; Withers, F.; Trichet, A. A. P.; Li, F.; Sich, M.; Del Pozo-Zamudio, O.; Clark, C.; Nalitov, A.; Solnyshkov, D. D. et al. Exciton-Polaritons in van Der Waals Heterostructures Embedded in Tunable Microcavities. *Nat. Commun.* **2015**, *6* (1), 1–7. https://doi.org/10.1038/ncomms9579.

(40) Liu, X.; Galfsky, T.; Sun, Z.; Xia, F.; Lin, E. C.; Lee, Y. H.; Kéna-Cohen, S.; Menon, V. M. Strong Light-Matter Coupling in Two-Dimensional Atomic Crystals. *Nat. Photonics* **2014**, *9* (1), 30. https://doi.org/10.1038/nphoton.2014.304.

(41) Liu, W.; Lee, B.; Naylor, C. H.; Ee, H. S.; Park, J.; Johnson, A. T. C.; Agarwal, R. Strong Exciton-Plasmon Coupling in MoS$_2$Coupled with Plasmonic Lattice. *Nano Lett.* **2016**, *16* (2), 1262–1269. https://doi.org/10.1021/acs.nanolett.5b04588.

(42) Liu, W.; Wang, Y.; Naylor, C. H.; Lee, B.; Zheng, B.; Liu, G.; Johnson, A. T. C.; Pan, A.; Agarwal, R. Understanding the Different Exciton-Plasmon Coupling Regimes in Two-Dimensional Semiconductors Coupled with Plasmonic Lattices: A Combined Experimental and Unified Equation of Motion Approach. *ACS Photonics* **2018**, *5* (1), 192–204. https://doi.org/10.1021/acsphotonics.7b00672.

(43) Cuadra, J.; Baranov, D. G.; Wersäll, M.; Verre, R.; Antosiewicz, T. J.; Shegai, T. Observation of Tunable Charged Exciton Polaritons in Hybrid Monolayer WS$_2$-Plasmonic Nanoantenna System. *Nano Lett.* **2018**, *18* (3), 1777–1785. https://doi.org/10.1021/acs.nanolett.7b04965.

(44) Zheng, D.; Zhang, S.; Deng, Q.; Kang, M.; Nordlander, P.; Xu, H. Manipulating Coherent Plasmon-Exciton Interaction in a Single Silver Nanorod on Monolayer WSe$_2$. *Nano Lett.* **2017**, *17* (6), 3809–3814. https://doi.org/10.1021/acs.nanolett.7b01176.

(45) Liu, B.; Fathi, M.; Chen, L.; Abbas, A.; Ma, Y.; Zhou, C. Chemical Vapor Deposition Growth of Monolayer WSe$_2$ with Tunable Device Characteristics and Growth Mechanism Study. *ACS Nano* **2015**, *9* (6), 6119–6127. https://doi.org/10.1021/acsnano.5b01301.

(46) Shi, H.; Yan, R.; Bertolazzi, S.; Brivio, J.; Gao, B.; Kis, A.; Jena, D.; Xing, H. G.; Huang, L. Exciton Dynamics in Suspended Monolayer and Few-Layer MoS$_2$ 2D Crystals. *ACS Nano* **2013**, *7* (2), 1072–1080. https://doi.org/10.1021/nn303973r.

(47) Rudin, S.; Reinecke, T. L. Anharmonic Oscillator Model for Driven and Vacuum-Field Rabi Oscillations. *Phys. Rev. B - Condens. Matter Mater. Phys.* **2001**, *63* (7), 075308. https://doi.org/10.1103/PhysRevB.63.075308.

(48) Khitrova, G.; Gibbs, H. M.; Kira, M.; Koch, S. W.; Scherer, A. Vacuum Rabi Splitting in Semiconductors. *Nat. Phys.* **2006**, *2* (2), 81–90. https://doi.org/10.1038/nphys227.

(49) Wang, W.; Vasa, P.; Pomraenke, R.; Vogelgesang, R.; De Sio, A.; Sommer, E.; Maiuri, M.; Manzoni, C.; Cerullo, G.; Lienau, C. Interplay between Strong Coupling and Radiative Damping of Excitons and Surface Plasmon Polaritons in Hybrid Nanostructures. *ACS Nano* **2014**, *8* (1), 1056–1064. https://doi.org/10.1021/nn405981k.

(50) Rempe, G.; Thompson, R. J.; Kimble, H. J. Cavity Quantum Electrodynamics with Strong Coupling in the Optical Domain. *Phys. Scr.* **1994**, *1994* (T51), 67. https://doi.org/10.1088/0031-8949/1994/T51/009.

(51) Savona, V.; Andreani, L. C.; Schwendimann, P.; Quattropani, A. Quantum Well Excitons in Semiconductor Microcavities: Unified Treatment of Weak and Strong Coupling Regimes. *Solid State Commun.* **1995**, *93* (9), 733–739. https://doi.org/10.1016/0038-1098(94)00865-5.

(52) Kewes, G.; Binkowski, F.; Burger, S.; Zschiedrich, L.; Benson, O. Heuristic Modeling of Strong Coupling in Plasmonic Resonators. *ACS Photonics* **2018**, *5* (10), 4089–4097. https://doi.org/10.1021/acsphotonics.8b00766.

(53) Fisher, T. A.; Afshar, A. M.; Whittaker, D. M.; Skolnick, M. S.; Roberts, J. S.; Hill, G.; Pate, M. A. Electric-Field and Temperature Tuning of Exciton-Photon Coupling in Quantum Microcavity Structures. *Phys. Rev. B* **1995**, *51* (4), 2600–2603. https://doi.org/10.1103/PhysRevB.51.2600.

(54) Koenderink, A. F. On the Use of Purcell Factors for Plasmon Antennas. *Opt. Lett.* **2010**, *35* (24), 4208–4210. https://doi.org/10.1364/ol.35.004208.

(55) Mann, J.; Sun, D.; Ma, Q.; Chen, J. R.; Preciado, E.; Ohta, T.; Diaconescu, B.; Yamaguchi, K.; Tran, T.; Wurch, M. et al. Facile Growth of Monolayer MoS$_2$ Film Areas on SiO$_2$. *Eur. Phys. J. B* **2013**, *86* (5), 226. https://doi.org/10.1140/epjb/e2013-31011-y.

(56) O'Brien, M.; McEvoy, N.; Hallam, T.; Kim, H. Y.; Berner, N. C.; Hanlon, D.; Lee, K.; Coleman, J. N.; Duesberg, G. S. Transition Metal Dichalcogenide Growth via Close Proximity Precursor Supply. *Sci. Rep.* **2014**, *4*, 7374. https://doi.org/10.1038/srep07374.

(57) Liu, M.; Guyot-Sionnest, P. Mechanism of Silver(I)-Assisted Growth of Gold Nanorods and Bipyramids. *J. Phys. Chem. B* **2005**, *109* (47), 22192–22200. https://doi.org/10.1021/jp054808n.

(58) Jana, N. R.; Gearheart, L.; Murphy, C. J. Seed-Mediated Growth Approach for Shape-Controlled Synthesis of Spheroidal and Rod-like Gold Nanoparticles Using a Surfactant Template. *Adv. Mater.* **2001**, *13* (18), 1389–1393. https://doi.org/10.1002/1521-4095(200109)13:18<1389::AID-ADMA1389>3.0.CO;2-F.

(59) Lee, C.; Yan, H.; Brus, L. E.; Heinz, T. F.; Hone, J.; Ryu, S. Anomalous Lattice Vibrations of Single- and Few-Layer MoS$_2$. *ACS Nano* **2010**, *4* (5), 2695–2700. https://doi.org/10.1021/nn1003937.

(60) Kang, Y.; Najmaei, S.; Liu, Z.; Bao, Y.; Wang, Y.; Zhu, X.; Halas, N. J.; Nordlander, P.; Ajayan, P. M.; Lou, J. et al. Plasmonic Hot Electron Induced Structural Phase Transition in a MoS$_2$ Monolayer. *Adv. Mater.* **2014**, *26* (37), 6467–6471. https://doi.org/10.1002/adma.201401802.

(61) Scheuschner, N.; Gillen, R.; Staiger, M.; Maultzsch, J. Interlayer Resonant Raman Modes in Few-Layer MoS$_2$. *Phys. Rev. B - Condens. Matter Mater. Phys.* **2015**, *91* (23), 235409. https://doi.org/10.1103/PhysRevB.91.235409.

(62) Lundt, N.; Klembt, S.; Cherotchenko, E.; Betzold, S.; Iff, O.; Nalitov, A. V.; Klaas, M.; Dietrich, C. P.; Kavokin, A. V.; Höfling, S. et al. Room-Temperature Tamm-Plasmon Exciton-Polaritons with a WSe$_2$ Monolayer. *Nat. Commun.* **2016**, *7* (1), 1–6. https://doi.org/10.1038/ncomms13328.

(63) Faucheaux, J. A.; Fu, J.; Jain, P. K. Unified Theoretical Framework for Realizing Diverse Regimes of Strong Coupling between Plasmons and Electronic Transitions. *J. Phys. Chem. C* **2014**, *118* (5), 2710–2717. https://doi.org/10.1021/jp412157c.

(64) Jung, G. H.; Yoo, S. J.; Park, Q. H. Measuring the Optical Permittivity of Twodimensional Materials without a Priori

Knowledge of Electronic Transitions. *Nanophotonics* **2018**, *8* (2), 263–270. https://doi.org/10.1515/nanoph-2018-0120.

(65) Wang, S.; Li, S.; Chervy, T.; Shalabney, A.; Azzini, S.; Orgiu, E.; Hutchison, J. A.; Genet, C.; Samorì, P.; Ebbesen, T. W. Coherent Coupling of WS_2 Monolayers with Metallic Photonic Nanostructures at Room Temperature. *Nano Lett.* **2016**, *16* (7), 4368–4374. https://doi.org/10.1021/acs.nanolett.6b01475.

(66) Chikkaraddy, R.; De Nijs, B.; Benz, F.; Barrow, S. J.; Scherman, O. A.; Rosta, E.; Demetriadou, A.; Fox, P.; Hess, O.; Baumberg, J. J. Single-Molecule Strong Coupling at Room Temperature in Plasmonic Nanocavities. *Nature* **2016**, *535* (7610), 127–130. https://doi.org/10.1038/nature17974.

(67) Wen, J.; Wang, H.; Wang, W.; Deng, Z.; Zhuang, C.; Zhang, Y.; Liu, F.; She, J.; Chen, J.; Chen, H. et al. Room-Temperature Strong Light-Matter Interaction with Active Control in Single Plasmonic Nanorod Coupled with Two-Dimensional Atomic Crystals. *Nano Lett.* **2017**, *17* (8), 4689–4697. https://doi.org/10.1021/acs.nanolett.7b01344.

(68) Rahman, D. S.; Chatterjee, H.; Ghosh, S. K. Excess Surface Energy at the Tips of Gold Nanospikes: From Experiment to Modeling. *J. Phys. Chem. C* **2015**, *119* (25), 14326–14337. https://doi.org/10.1021/acs.jpcc.5b03944.

(69) Hanlon, D.; Backes, C.; Higgins, T. M.; Hughes, M.; O'Neill, A.; King, P.; McEvoy, N.; Duesberg, G. S.; Mendoza Sanchez, B.; Pettersson, H.; et al. Production of Molybdenum Trioxide Nanosheets by Liquid Exfoliation and Their Application in High-Performance Supercapacitors. *Chem. Mater.* **2014**, *26* (4), 1751–1763. https://doi.org/10.1021/cm500271u.

(70) Kékicheff, P.; Spalla, O. Refractive Index of Thin Aqueous Films Confined between Two Hydrophobic Surfaces. *Langmuir* **1994**, *10* (5), 1584–1591. https://doi.org/10.1021/la00017a043.

(71) Johnson, P. B.; Christy, R. W. Optical Constants of the Noble Metals. *Phys. Rev. B* **1972**, *6* (12), 4370. https://doi.org/10.1103/PhysRevB.6.4370.